Maneuver and Vibration Control of SCOLE

R. D. Quinn* and L. Meirovitch†
Virginia Polytechnic Institute and State University, Blacksburg, Virginia

This paper is concerned with the simultaneous maneuver and vibration control of the Spacecraft Control Laboratory Experiment (SCOLE). The approach is based on a perturbation method permitting a maneuver strategy independent of the vibration control. Some of the problems encountered in dynamical modeling of a flexible spacecraft in an Earth-based laboratory are highlighted and solved. Numerical results demonstrating rotational maneuvers and vibration control of the SCOLE model are included.

I. Introduction

THE problem of simultaneous maneuver and vibration suppression of spacecraft is becoming increasingly important. Some NASA projects involve experiments consisting of the control of flexible bodies carried by a shuttle in an Earth orbit. Other projects, such as the Spacecraft Control Laboratory Experiment (SCOLE), involve laboratory simulations of similar experiments. The equations of motion for both types of experiments have been presented previously.[1] Also in Ref. 1, a perturbation technique was presented permitting the formulation of a maneuver strategy independent of the vibration problem. Maneuver and vibration control strategies based on the perturbation technique of Ref. 1 have been presented in Refs. 2 and 3. Reference 3 is concerned with simulation in space, whereas this paper is concerned with problems encountered in an Earth-based laboratory simulation.

Turner and Junkins,[4] Breakwell,[5] and Turner and Chun[6] addressed the problem of rotational maneuvering and simultaneous vibration suppression of flexible spacecraft for two-dimensonal models. In all cases, the methods used represent extensions of rigid-body maneuvering techniques, requiring the solution of a two-point boundary-value problem. The maneuver and vibration control problems are coupled, and numerical difficulties arise as the order of the system increases.[5] Baruh and Silverberg first suggested separating the maneuver and vibration control problems.[7] However, the vibration control did not include feedback control of the rigid-body modes as well, so that the spacecraft orientation could not be corrected during the open-loop maneuver.

Laboratory experiments in the control of flexible structures have been concerned with vibration suppression of beams and grids.[8,9] The grid structure of Ref. 9 was suspended by means of cables, so that it experienced a pendulum mode. The SCOLE program is a logical extension of the efforts of Refs. 8 and 9 to three-dimensional structures.

The SCOLE project is a precursor of the Control of Flexible Spacecraft (COFS) project, where the latter consists of the control of flexible bodies carried in an Earth orbit as well as associated Earth-based laboratory experimentation. Because it is almost impossible to duplicate the space environment in a laboratory, it is important to identify difficulties likely to be encountered in dynamical simulation of spacecraft control in the laboratory and to develop ways of overcoming them.

This paper is concerned with the simultaneous maneuver and vibration control of the model used in SCOLE. The paper contains summaries of the equations of motion and of a perturbation technique permitting the design of a maneuver strategy independent of the vibration control. Some of the problems unique to an Earth-based laboratory simulation of maneuvering a three-dimensional flexible spacecraft are highlighted and solved.

A spacecraft has six rigid-body degrees of freedom, three rotations, and three translations (Fig. 1). However, the laboratory model is constrained by a support cable attached by means of a universal joint (Fig. 2). Hence, the support allows rotational freedom of movement but limits the rigid-body translational motions. For an orbiting spacecraft, a centrifugal force distributed over the structure balances most of the distributed gravitational force. In the laboratory, the cable balances the distributed gravitational force at a single point, so that the laboratory model displays a more pronounced static deformation pattern. Moreover, the location of the universal joint greatly affects the stability of the model.

In the derivation of the equations of motion for the SCOLE model of Fig. 2, the shuttle is treated as a rigid body and the beam, antenna, and cable as flexible distributed-parameter members. The motion is described by means of a reference frame $x_O y_O z_O$ attached to the shuttle, so that the motion of the frame $x_O y_O z_O$ is regarded as rigid-body motion and displacements relative to $x_O y_O z_O$ as elastic motion. The magnitude of the rigid-body rotations is not restricted, but the elastic displacements are assumed to remain in the linear range. Hence, the equations of motion are nonlinear in the variables describing the motion of the body-fixed reference frame. The structural model is discretized and truncated by representing the elastic motion in terms of a finite set of admissible functions.[10]

A first-order perturbation approach to the solution of the equations of motion is presented. This technique amounts to separating the equations of motion into a set of equations governing the rigid-body motions and a set of time-varying linear equations governing small elastic motions and perturbations from the prescribed rigid-body maneuver, where the latter represents a regulator problem. The perturbation technique permits a maneuver strategy that is independent of the elastic motion. The time-varying coefficients for the perturbation equations are known as soon as the rigid-body maneuver policy has been determined. The actual controls are obtained by summing up the contributions from both the rigid-body maneuvering and the regulator problem.

The effects of the cable and the gravitational stiffening on the eigensolution of the laboratory model are examined. A stability analysis proves very valuable in minimizing the control effort and at the same time assures safety during the maneuver. The maneuver and vibration control methods of Refs. 2 and 3 are found to be effective, but gravity requires

Received June 15, 1987; revision received Sept. 31, 1987.

*Graduate Research Assistant, Department of Engineering Science and Mechanics; currently, General Motors Assistant Professor, Department of Mechanical and Aerospace Engineering, Case Western Reserve University, Cleveland, OH.

†University Distinguished Professor, Department of Engineering Science and Mechanics. Fellow AIAA.

separate shape control if the configuration of the model is to be maintained precisely. Shape control during the maneuver requires more actuators than mere vibration control. Numerical results demonstrating the maneuver and vibration control of the SCOLE are presented.

II. Equations of Motion

It is convenient to refer the motion of a spacecraft to a reference frame $x_O y_O z_O$ embedded in the undeformed structure (Fig. 1). In a space environment, the reference frame has six degrees of freedom, three rigid-body rotations, and three rigid-body translations. In the laboratory experiment, the spacecraft is not actually free in space, but suspended from the ceiling by means of a cable. The cable is attached to the spacecraft through a universal joint, which does not restrict rotational motion. The cable acts like an elastic member. The equations of motion are obtained by means of the Lagrangian approach. To this end, we must derive expressions for the kinetic energy, potential energy, and virtual work.

Considering Fig. 2, the position vector for an arbitrary point C on the cable relative to the inertial coordinate system is $\boldsymbol{R}_C = \boldsymbol{c} + \boldsymbol{w}$, where $\boldsymbol{c}$ is the nominal position of a point on the cable and $\boldsymbol{w}$ is the elastic displacement of the point. The position vector of the point of support of the shuttle, point O, is $\boldsymbol{R} = \boldsymbol{c}_B + \boldsymbol{w}_B + \boldsymbol{e}$, where $\boldsymbol{e}$ is the vector from the universal joint, point B, to point O. The position of a point S in the rigid shuttle relative to the inertial frame XYZ is $\boldsymbol{R}_S = \boldsymbol{R} + \boldsymbol{r}$, where $\boldsymbol{r}$ is the nominal position of S relative to O, and the position of a point A on the appendage is $\boldsymbol{R}_A = \boldsymbol{R} + \boldsymbol{a} + \boldsymbol{u}$, where $\boldsymbol{a}$ is the nominal position of A relative to O and $\boldsymbol{u}$ is the elastic displacement of A. The velocities of these points are $\dot{\boldsymbol{R}}_C = \dot{\boldsymbol{w}}$, $\dot{\boldsymbol{R}}_S = \dot{\boldsymbol{R}} + \boldsymbol{\omega} \times \boldsymbol{r}$, and $\dot{\boldsymbol{R}}_A = \dot{\boldsymbol{R}} + \boldsymbol{\omega} \times (\boldsymbol{a} + \boldsymbol{u}) + \dot{\boldsymbol{u}}$, where $\dot{\boldsymbol{R}} = \dot{\boldsymbol{w}}_B + \boldsymbol{\omega} \times \boldsymbol{e}$ in which $\boldsymbol{\omega}$ is a vector of angular velocities of the body-fixed frame $x_O y_O z_O$ with respect to the inertial frame and $\dot{\boldsymbol{u}}$ and $\dot{\boldsymbol{w}}$ are the elastic velocities relative to $x_O y_O z_O$ of points on the appendage and cable, respectively.

To derive Lagrange's equations of motion, the kinetic energy, potential energy, and virtual work were expressed in terms of a consistent set of components about the body axes $x_O y_O z_O$ by introducing a rotational transformation matrix C from the inertial frame XYZ to the body axes, where the elements of C are functions of a given set of Euler's angles α_1, α_2, and α_3. Moreover, to obtain Lagrange's equations of motion in terms of the Euler angles $\alpha_1, \alpha_2, \alpha_3$, the relationship

$$\boldsymbol{\omega} = D(\alpha_1, \alpha_2, \alpha_3)\,\dot{\boldsymbol{\alpha}} \tag{1}$$

between the vector $\boldsymbol{\omega}$ of body-fixed angular velocities and the vector $\dot{\boldsymbol{\alpha}}$ of time rate of change of the Euler angles was used, where $D(\alpha_1, \alpha_2, \alpha_3)$ is a 3×3 transformation matrix. Finally, the system was discretized in space by expressing the elastic displacement vectors in the form

$$\boldsymbol{u} = \Phi \boldsymbol{q}, \qquad \boldsymbol{w} = \psi \boldsymbol{\eta} \tag{2}$$

where Φ and ψ are matrices of space-dependent admissible functions and $\boldsymbol{q}$ and $\boldsymbol{\eta}$ are vectors of time-dependent generalized coordinates.

Lagrange's equations were derived as in Ref. 1. For large rigid-body motions, they represent a set of simultaneous nonlinear ordinary differential equations. The complete nonlinear equations are not given here for brevity. In the next section, we present the perturbation scheme and the resulting perturbation equations.

III. Perturbation Method

Let us assume that Euler's angles can be written in the form

$$\alpha_i = \alpha_{0i} + \alpha_{1i}, \qquad i = 1,2,3 \tag{3}$$

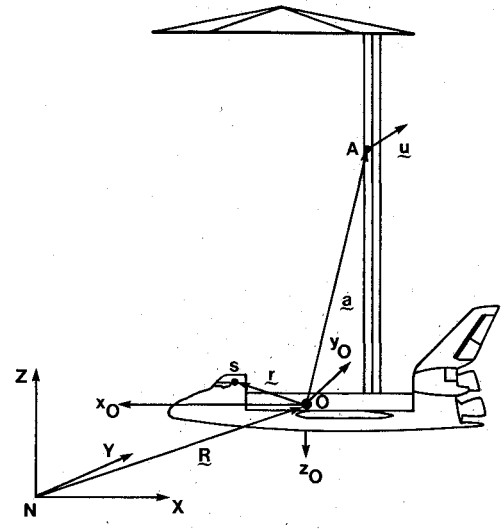

Fig. 1 The SCOLE model in space.

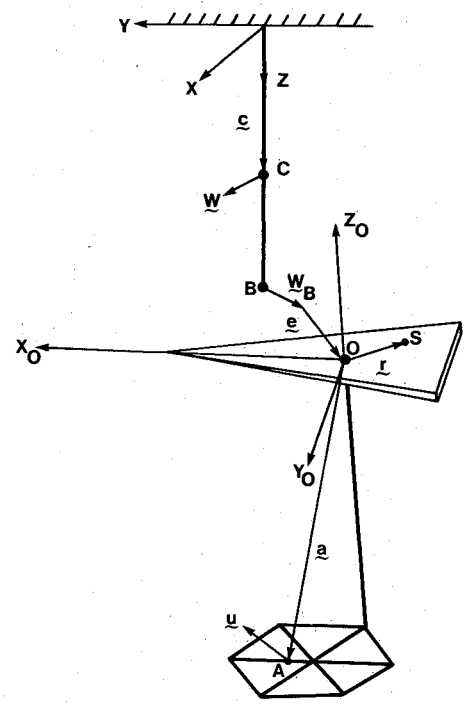

Fig. 2 Laboratory model of the SCOLE.

where α_{0i} are the unperturbed angles, regarded as the zero-order quantities, and α_{1i} are first-order perturbations, which implies that α_{1i} are one order of magnitude smaller than α_{0i}. Introducing Eqs. (3) into the nonlinear equations of motion and separating orders of magnitude, we obtain unperturbed zero-order equations and first-order perturbation equations. Moreover, we assume that the elastic displacements of the cable and appendage are of first order in magnitude. Before proceeding with this technique, we first develop some expressions relating the perturbations in the Euler angles with small angular deflections β_1, β_2, and β_3 expressed in the body-fixed frame. This will permit expressing all the variables in the perturbation equations describing the motion of the spacecraft in terms of components along the $x_O y_O z_O$ frame.

It can be shown that the vector $\boldsymbol{\beta}$ of body-fixed perturbation angles can be related to the vector $\boldsymbol{\alpha}_1$ of perturbed Euler angles by

$$\boldsymbol{\beta} = D(\alpha_{01}, \alpha_{02}, \alpha_{03})\,\boldsymbol{\alpha}_1 \tag{4}$$

where the structure of $D(\alpha_{01}, \alpha_{02}, \alpha_{03})$ is the same as the structure of $D(\alpha_1, \alpha_2, \alpha_3)$ in Eq. (1). The perturbed angular velocity vector can then be expressed as

$$\omega \cong \omega_0 + \omega_1, \qquad \omega_1 = \tilde{\omega}_0^T \beta + \dot{\beta} \tag{5}$$

where the tilde over a symbol, such as in $\tilde{\omega}_0^T$, denotes the matrix equivalent of the vector product $\omega_0 \times$ (see Ref. 1). The applied forces and moments entering into the equations for the rigid-body motion can also be expressed in first-order perturbed form as follows:

$$F = F_0 + F_1, \qquad M = M_0 + M_1 \tag{6}$$

The zero-order equations of motion, governing the structure as if it were rigid, can be expressed as[1]

$$I_B \dot{\omega}_0 + \tilde{\omega}_0^T I_B \omega_0 = M_0 \tag{7}$$

where I_B is the mass moment of inertia matrix about the universal joint. The first-order linear equations governing the vibrational motion of the structure and the perturbations in the rigid-body maneuver can be expressed in the matrix form[1]

$$M\ddot{x} + G\dot{x} + (K_S + K_{NS})x = F^* \tag{8}$$

where

$$x^T = [\eta^T | \beta^T | q^T], \tag{9a}$$

$$F^{*T} = [F_0^T + \psi_B F_1^T | M_0'^T + M_1^T | Q_0^T + Q_1^T] \tag{9b}$$

$$M = \left[\begin{array}{c|c|c} M_C & \psi_B^T \tilde{S}_B & \psi_B^T \bar{\Phi} \\ \hline \tilde{S}_B^T \psi_B & I_B & \tilde{\Phi} \\ \hline \bar{\Phi}^T \psi_B & \tilde{\Phi}^T & M_A \end{array}\right] \tag{9c}$$

$$G = \left[\begin{array}{c|c|c} 2\tilde{L}_C & 2\psi_B^T \tilde{\omega}_0^T \tilde{S}_B & 2\psi_B^T \tilde{\omega}_0^T \bar{\Phi} \\ \hline -2\left(\psi_B^T \tilde{\omega}_0^T \tilde{S}_B\right)^T & I_B \tilde{\omega}_0^T + \tilde{\omega}_0^T I_B + \widetilde{[I_B \omega_0]} & \tilde{\omega}_0^T \tilde{\Phi} + J_0 \\ \hline -2\left(\psi_B^T \tilde{\omega}_0^T \bar{\Phi}\right)^T & -\left[\tilde{\omega}_0^T \tilde{\Phi} + J_0\right]^T & 2\tilde{L}_A \end{array}\right] \tag{9d}$$

$$K_S = \left[\begin{array}{c|c|c} \bar{L}_C + K_C & \psi_B^T \tilde{\omega}_0^2 \tilde{S}_B & \psi_B^T \tilde{\omega}_0^2 \bar{\Phi} \\ \hline \tilde{S}_B^T \tilde{\omega}_0^2 \psi_B & \tilde{\omega}_0 I_B \tilde{\omega}_0 & \tilde{\omega}_0^T J_0 + \widetilde{[C_0 g]} \bar{\Phi} \\ \hline \bar{\Phi}^T \tilde{\omega}_0^2 \psi_B & J_0^T \tilde{\omega}_0 + \bar{\Phi}^T \widetilde{[C_0 g]}^T & \bar{L}_A + K_A \end{array}\right] \tag{9e}$$

$$K_{NS} = \left[\begin{array}{c|c|c} \tilde{L}_C & \psi_B^T \dot{\tilde{\omega}}_0^T \tilde{S}_B & \psi_B^T \dot{\tilde{\omega}}_0^T \bar{\Phi} \\ \hline -\left(\psi_B^T \dot{\tilde{\omega}}_0^T \tilde{S}_B\right)^T & I_B \dot{\tilde{\omega}}_0^T + \widetilde{[I_B \omega_0]} \tilde{\omega}_0^T + \tilde{S}_B \widetilde{[C_0 g]} & \dot{J}_0 \\ \hline -\left(\psi_B^T \dot{\tilde{\omega}}_0^T \bar{\Phi}\right)^T & \tilde{\Phi}^T \dot{\tilde{\omega}}_0^T & \tilde{L}_A \end{array}\right] \tag{9f}$$

and

$$\bar{\Phi} = \int_{m_A} \Phi \, dm_A, \qquad \bar{\psi} = \int_{m_C} \psi \, dm_C, \qquad \tilde{\Phi}^T = \int_{m_A} \Phi^T \tilde{b} \, dm_A \tag{10a}$$

$$\tilde{L}_A = \int_{m_A} \Phi^T \tilde{\omega}^T \Phi \, dm_A, \qquad \bar{L}_A = \int_{m_A} \Phi^T \tilde{\omega}^2 \Phi \, dm_A \tag{10b}$$

$$\tilde{L}_C = \int_{m_C} \psi^T \tilde{\omega}^T \psi \, dm_C, \qquad \bar{L}_C = \int_{m_C} \psi^T \tilde{\omega}^2 \psi \, dm_C \tag{10c}$$

$$M_A = \int_{m_A} \Phi^T \Phi \, dm_A, \qquad M_C = \int_{m_C} \psi^T \psi \, dm_C + m\psi_B^T \psi_B \tag{10d}$$

$$J_0 = \int_{m_A} \left(\tilde{a}\tilde{\omega}_0 + \widetilde{[a\omega_0]}\right) \Phi \, dm_A, \qquad C_0 = C(\alpha_0) \tag{10e}$$

$$S_B = \int_{m_S} r \, dm_S + \int_{m_A} a \, dm_A + me, \qquad b = a + e \tag{10f}$$

in which m_C, m_A, m_S, and m are the masses of the cable, appendage, shuttle, and total spacecraft, respectively. Moreover, K_C and K_A are the elastic stiffness of the cable and appendage, respectively. The disturbing forces on the right side of Eq. (9b) take the form

$$F_0 = -\psi_B^T \left[\tilde{\omega}_0^T \tilde{S}_B \omega_0 + \tilde{S}_B \dot{\omega}_0\right] - \left(m\psi_B^T + \bar{\psi}^T\right) C_0 g \tag{11a}$$

$$M_0' = \tilde{S}_B C_0 g \tag{11b}$$

$$Q_0 = -\left[\tilde{\Phi}^T \dot{\omega}_0 + \int_{m_A} \Phi^T \tilde{\omega}_0^T \tilde{b} \omega_0 \, dm_A + \bar{\Phi}^T C_0 g\right] \tag{11c}$$

where g is a vector in the Z direction of magnitude equal to the acceleration due to gravity. We observe that F_1, M_1, and Q_1 are vectors of external generalized forces associated with the perturbations in the rigid-body translations, rigid-body rotations, and elastic displacements, respectively. In view of Eqs. (11), there are three types of disturbing forces causing undesirable motion of the structure during a maneuver: tangential and centrifugal forces, resulting from the motion of the body-fixed frame, and gravitational. Correspondingly, we will use three types of active control methods to suppress the effect of these disturbances: maneuver control to produce gross motion, but applied in a manner that partially offsets the tangential and centrifugal forces, shape control to suppress the effect of gravity, and vibration control to provide damping and suppress the effects of the remaining disturbing forces. The control forces affecting the elastic motion are denoted by the vector Q_1 in the second part of Eq. (9b) and contain contributions from the maneuver, shape, and vibration control.

IV. Rigid-Body Rotations

The perturbation method permits an open-loop maneuver strategy that is independent of the vibration problem. However, small perturbations from the rigid-body maneuver can be suppressed by means of closed-loop vibration control. Hence, the maneuver strategy can be formulated in a straightforward manner. Indeed, a single-axis minimum-time maneuver strategy is developed in Ref. 2. With this method, the axis of rotation need not be a principal axis, so that any general rotation is possible. The maneuver policy is formulated in continuous time but implemented in discrete time so that some error can occur. However, the vibration control includes feedback control of the rigid-body modes and can reduce this erorr.

The most desirable control technique for a maneuver excites only the desired rigid-body motion, not the elastic modes. From Ref. 2, the components of the force distribution exhibiting these characteristics can be expressed as

$$F_1(p,t) = x(p)m(p)\dot{\theta}^2(t) \tag{12a}$$

$$F_2(p,t) = -z(p)m(p)\ddot{\theta}(t) \tag{12b}$$

$$F_3(p,t) = y(p)m(p)\ddot{\theta}(t) \tag{12c}$$

where $\theta(t)$ is the desired angular motion, $m(p)$ is the mass density at point p, and $x(p)$, $y(p)$, and $z(p)$ are the components of the position vector of point p with respect to the center of mass. The actuator forces are proportional to rotational rigid-body modes, so that they will not excite the elastic modes and cause undesirable vibration. Another perspective, gained from Eqs. (11), is that the maneuver control forces of Eqs. (12b) and (12c) cancel the tangential disturbing force, and the force given by Eq. (12a) partially cancels the centrifugal disturbing force. Of course, distributed forces can only be implemented approximately with discrete actuators, which tend to excite some vibration. Also, centrifugal forces can cause vibration during the maneuver, so that vibration control may be necessary. Before proceeding with the vibration analysis, it is necessary to perform a static analysis to determine the equilibrium position and stability characteristics of the system.

V. Static Analysis

For safety, the laboratory experiment must be designed so that the structure is stable at all times. This means that when the structure is rotated to its maximum maneuver angle, it will remain in this orientation or, at worst, oscillate about its initial position if no external torques are applied. For stability of the SCOLE model, the universal joint must be located at or above the true center of mass of the system at all times. Of course, the true center of mass changes with elastic deformation. Hence, the location of the universal joint must be chosen very carefully. A static analysis is useful for checking the stability of the mathematical model and for adjusting the location of the universal joint in an iterative fashion to achieve stability at the desired orientation.

Gravity has a much stronger influence in the laboratory experiment because the balancing force is a point (cable) force rather than a body (centrifugal) force as with the orbiting structure. It is assumed that the universal joint is in the vicinity of the rigid-body center of mass along the axes orthogonal to the cable. That is, point B is near the center of mass and perhaps somewhere above it. We now wish to find the stable equilibrium orientation and elastic deflection of the structure for a given joint location. For the laboratory experiment, the static portions of Eqs. (8-11) can be expressed as

$$K_{ST}x_{ST} = F_{ST} \tag{13a}$$

where the static stiffness matrix is

$$K_{ST} = \begin{bmatrix} K_C & 0 & 0 \\ 0 & \tilde{S}_B[\widetilde{C_0 g}] & [\widetilde{C_0 g}]\bar{\Phi} \\ 0 & \bar{\Phi}^T[\widetilde{C_0 g}]^T & K_A \end{bmatrix} \tag{13b}$$

and the static force is

$$F_{ST} = \begin{bmatrix} -\left(m\Phi_B^T + \bar{\psi}^T\right)C_0 g \\ \tilde{S}_B C_0 g \\ -\bar{\Phi}^T C_0 g \end{bmatrix} \tag{13c}$$

Equations (13) form a set of nonlinear algebraic equations that can be solved for x_{ST}, i.e., for the static equilibrium orientation and elastic deflection of the structure. The elastic deflection is coupled with the angular orientation of the structure. The orientation about the longitudinal axis of the cable (direction of gravity) is arbitrary. This means that a rotation about this axis will not affect the static orientation or elastic deflections. Any orientation can be made to coincide with the stable equilibrium position by properly locating the universal joint using Eqs. (13). Hence, a single-axis rotation not affected by gravity can be accomplished about any desired axis of the spacecraft once the proper joint location has been determined.

VI. Quasimodal Equations of Motion

During the maneuver, the gyroscopic and stiffness matrices, and hence the eigenvalue problem, are functions of time. In Ref. 2, a truncated set of premaneuver eigenvectors is used as a set of admissible vectors to simplify and reduce the order of the equations of motion to a form called the "quasimodal" equations of motion. Using this approach, Eq. (8) can be reduced to the quasimodal form

$$\ddot{u}(t) + \bar{G}(t)\dot{u}(t) + [\Lambda + K(t)]u(t) = f^*(t) \tag{14}$$

where u is a vector of quasimodal coordinates defined by

$$x(t) = Xu(t) \tag{15}$$

where X is a rectangular matrix of the lower premaneuver eigenvectors normalized so that

$$X^T M X = I, \qquad X^T K_0 X = \Lambda \tag{16}$$

in which K_0 is the constant part of the stiffness matrix, Λ is a diagonal matrix of the premaneuver eigenvalues, and

$$\bar{G}(t) = X^T G(t) X, \qquad \bar{K}(t) = X^T K_t(t) X \tag{17}$$

are reduced-order gyroscopic and stiffness matrices in which $K_t(t)$ is the time-dependent part of the stiffness matrix. Moreover,

$$f^*(t) = X^T F^*(t) \tag{18}$$

is the vector of quasimodal forces. Comparing Eq. (14) with Eq. (8), we see that the premaneuver eigenvectors have not decoupled the equations of motion. However, as the maneuver velocity decreases, the time-varying terms decrease in magnitude and the equations approach an uncoupled form. Also note that the mass matrix has been reduced to the identity matrix, which is convenient for casting Eq. (14) in state space form. Note that the mass of the cable has been neglected, which will be shown to be an acceptable assumption.

VII. Vibration Control

The tangential and centrifugal disturbing forces can cause vibration during the maneuver, as demonstrated in Ref. 2. The perturbation method permits the vibration control to be formulated separately from the manuever control. Pole placement and optimal vibration control techniques are developed in Ref. 3. The vibration control laws are formulated using the premaneuver eigensolution. Because the eigensolution is time-varying during the maneuver, the premaneuver eigenvectors act only as admissible vectors for vibration control. *The time-varying terms have been ignored only in the design of the feedback controls. The complete quasimodal equations, including the time-varying terms, are used in the computer simulations of the equations.* Actuator dynamics was found to degrade vibration control performance. The inclusion of the actuator dynamics in the control formulation, along with structural dynamics, helps minimize this degradation.

The equation governing the actuators' response is assumed to have the vector form

$$\dot{F}(t) = aF(t) + bF_c(t) \tag{19}$$

where a and b are constants, F is the control force vector (output of the actuators), and F_c is the command force vector (input to the actuators). If the actuator equations of motion

are inserted into the structural equations of motion, then the equation governing the rth premaneuver mode becomes

$$\dot{z}_r = A_r z_r + b f_{cr} \tag{20}$$

where

$$z_r^T = [u_r\ \dot{u}_r\ \ddot{u}_r], \qquad b^T = [0\ 0\ b] \tag{21}$$

$$A_r = \begin{bmatrix} 0 & 1 & 0 \\ 0 & 0 & 1 \\ a\omega_r^2 & -\omega_r^2 & a \end{bmatrix} \tag{22}$$

in which u_r and ω_r are the rth premaneuver modal displacement and natural frequency, respectively.

For optimal control, the performance index can be chosen as a weighted sum of the elastic kinetic and potential energy and control effort. In the independent modal space control (IMSC) method, also known as natural control,[11,12] this performance index has the form

$$J = \sum_{r=1}^{\infty} J_r \tag{23}$$

where

$$J_r = \int_0^{\infty} \left(z_r^T Q_r z_r + R_r f_{cr}^2 \right) dt \tag{24a}$$

are modal performance indices, in which

$$Q_r = \begin{bmatrix} q_r & 0 & 0 \\ 0 & 1 & 0 \\ 0 & 0 & 0 \end{bmatrix} \tag{24b}$$

is a weighting matrix and R_r is a weighting factor. For elastic modes, q_r is taken as the rth eigenvalue ω_r^2, and for rigid-body modes, q_r is chosen on the basis of pole placement considerations. The choice of the weight R_r is based on the available control command force for vibration suppression. The rth modal gains, denoted by g_{r1}, g_{r2}, and g_{r3}, are determined by solving an algebraic matrix Riccati equation of order three. Note that this implies that the time available for control is infinitely large, as indicated by the upper limit in the integral in Eq. (24a), and that the gains are constant. The feedback control law for the rth mode is simply

$$f_{cr} = -g_{r1} u_r - g_{r2} \dot{u}_r - g_{r3} \ddot{u}_r \tag{25}$$

Introducing Eq. (25) into Eq. (20), considering Eqs. (21) and expanding the characteristic determinant, we conclude that the closed-loop poles must satisfy the equation

$$s^3 + (b g_{r3} - a) s^2 + (b g_{r2} + \omega_r^2) s + (b g_{r1} - a\omega_r^2) = 0 \tag{26}$$

In the pole allocation method, the modal gains are chosen to produce the desired closed-loop poles. The closed-loop poles for the rth mode can be expressed in the general form

$$s_{r1} = \rho_r + i\xi_r, \qquad s_{r2} = \rho_r - i\xi_r, \qquad s_{r3} = \gamma_r \tag{27}$$

where ρ_r and γ_r are the decay rates of the rth mode and ξ_r is the closed-loop modal frequency. The characteristic equation associated with the poles given by Eq. (27) is

$$s^3 - (\gamma_r + 2\rho_r) s^2 + (2\gamma_r \rho_r + \rho_r^2 + \xi_r^2) s - \gamma_r (\rho_r^2 + \xi_r^2) = 0 \tag{28}$$

Comparing Eqs. (26) and (28), we obtain the control gains

$$g_{r1} = \frac{1}{b} \left[a\omega_r^2 - \gamma_r (\rho_r^2 + \xi_r^2) \right] \tag{29a}$$

$$g_{r2} = \frac{1}{b} (2\gamma_r \rho_r + \rho_r^2 + \xi_r^2 - \omega_r^2), \qquad g_{r3} = \frac{1}{b} (a - 2\rho_r - \gamma_r) \tag{29b}$$

Hence, the poles given by Eqs. (27) can be chosen for each mode and implemented with the modal force of Eq. (25) and the gains of Eqs. (29).

Modal control techniques have become quite common in control of structures because of their ability to take advantage of the physical and mathematical properties of the natural modes of vibration. The main drawback common to all modal control methods is the problem of modal state estimation with discrete sensors. In this investigation, modal observability is assumed. Direct feedback, where the command control force is related directly to the measured state through control gains, avoids modal estimation entirely. In addition, if this feedback force is a physical (rather than a modal) force, then a modal force implementation is also avoided. Hence, a useful control technique might take advantage of the concept of natural modes while still being applicable to output feedback. One such method is known as uniform damping control.[13]

Consider a linear control law having the special form

$$\boldsymbol{F}_c(t) = -A[\boldsymbol{x}(t) g_1 + \dot{\boldsymbol{x}}(t) g_2 + \ddot{\boldsymbol{x}}(t) g_3] \tag{30}$$

where g_1, g_2 and g_3 are control gain factors, $\boldsymbol{F}_c$ is a vector of actual command forces, $\boldsymbol{x}$, $\dot{\boldsymbol{x}}$, and $\ddot{\boldsymbol{x}}$ are vectors of measured displacements, velocities, and accelerations, and A is a weighting matrix of constant coefficients. It was shown in Ref. 3 that if the force vector of Eq. (30) is to be produced by modal command forces of the form

$$f_c(t) = -\boldsymbol{u}(t) g_1 - \dot{\boldsymbol{u}}(t) g_2 - \ddot{\boldsymbol{u}}(t) g_3 \tag{31}$$

where the modal gains are the same for all modes, then the weighting matrix A must be equal to the mass matrix M of the structure.

For uniform damping control, the modal gains given by Eq. (29) are chosen so that all the modes decay at the same rate ρ. If, in addition, the gains are chosen so that the closed-loop modal frequencies of vibration ξ_r are equal to the open-loop (natural) frequencies ω_r, then the modal gains are the same for all the modes. The gain factors for uniform damping control can be verified to have the form[3]

$$g_1 = -a\rho^2/b, \qquad g_2 = \rho(2a + \rho)/b, \qquad g_3 = -2\rho/b \tag{32}$$

and the corresponding control law is given by Eq. (30) with the matrix A replaced by M, or

$$\boldsymbol{F}_c(t) = -M[\boldsymbol{x}(t) g_1 + \dot{\boldsymbol{x}}(t) g_2 + \ddot{\boldsymbol{x}}(t) g_3] \tag{33}$$

As with other distributed control techniques, uniform damping control can only be implemented approximately with discrete actuators. However, this control method has the advantage of being applicable to direct feedback control, with collocated actuators and sensors, and one that is known to be robust.[13] If an actuator and sensor pair is located at node i, acting in direction ℓ, the control command force at that location takes the form

$$F_{i\ell} = -m_{i\ell} (x_{i\ell} g_1 + \dot{x}_{i\ell} g_2 + \ddot{x}_{i\ell} g_3) \tag{34}$$

where $m_{i\ell}$ is an entry of the mass matrix and $x_{i\ell}$, $\dot{x}_{i\ell}$, and $\ddot{x}_{i\ell}$ are counterparts of displacement, velocity, and acceleration vectors, respectively, all of which correspond to node i and direction ℓ. This is known as decentralized control because the force at a point is related only to measurements taken at that point and, of course, is only possible when the actuators and sensors are collocated.

VIII. Shape Control

One part of the SCOLE design challenge requires rotating the structure through a specified angle and then aiming the antenna within a certain tolerance, all in minimum time. Hence, for SCOLE, the control task of highest priority is aiming the antenna and maintaining its shape. The shape of the mast is not critical, provided its deformation is within reasonable limits. Shape control implies suppressing the effect of a steady-state or a slowly varying force by maintaining approximately a certain mean configuration. On the other hand, vibration control suppresses small motions of the structure about the desired steady-state configuration. Hence, the purpose of shape control is to add stiffness to the structure, while that of vibration control is to provide damping. Shape control can adjust the orientation and position of the $x_O y_O z_O$ frame as well as shape the structure elastically.

If the axis of rotation does not correspond to the gravitational axis, the static deformation varies with time during the maneuver. Hence, in aiming the antenna, the static deformation due to gravity must be taken into consideration. One possibility is to attempt to suppress the static deformation with active controls, i.e., to keep the entire structure undeformed. This is total structural shape control and may be necessary if the antenna is to be oriented accurately and uniformly with respect to the shuttle. An alternative approach is to attempt to control the shape and orientation of the antenna only, allowing the mast to deform.

Shape control requires a control force equal and opposite to the disturbing forces. Gravity is a distributed force, and its effect should be suppressed by a distributed force, or at least by a force generated by a large number of discrete actuators. For a spacecraft in orbit, the gravitational force is largely cancelled by a distributed centrifugal force, and only higher-order effects such as the gravity gradient, aerodynamic drag, and solar wind forces must be combated with shape control forces. However, for the laboratory model, only the tether tension, which is a point force, opposes gravity. Hence, shape control requires more control effort for the laboratory model than for an orbiting spacecraft. In fact, typical vibration control techniques, such as those considered here, include feedback on the displacement and are capable of the higher-order shape control required for an orbiting spacecraft.

Gravity provides a steady-state disturbing force depending only on the mass distribution of the structure, as can be seen in Eq. (11). The mass distribution is generally known more accurately than the stiffness distribution. Hence, shape control can be open-loop in some circumstances, such as in the laboratory. However, for an orbiting spacecraft, the steady-state forces are less well defined, though smaller in magnitude, and require closed-loop control.

Due to the large amount of effort and the large number of actuators required, precise shape control may be impractical for the laboratory experiment. An alternative is to implement only vibration control, i.e., to allow the structure to deform statically during the maneuver but suppress the vibrations about this configuration. Vibration control of this type can be formulated by including the gravitational potential along with the elastic potential energy in the performance functional discussed in Sec. VII.

IX. Numerical Results

A. Mathematical Model

The SCOLE configuration of Fig. 2 is modeled by means of the finite-element method. The mast supporting the antenna is a steel tube 10 ft in length. The antenna consists of 12 aluminum tubes, each 2 ft long, welded together to form a grid in a hexagonal shape. The tether is an 11-ft-long steel cable. The material properties can be found in Table 1. There is a lumped mass of 0.01719 slugs at the point of attachment of the antenna to the mast. Also, the hub of the antenna is considered to be a lumped mass of 0.004201 slugs. Figure 3 shows the nodal locations of the finite-element model. Hermite cubics[10] were used as interpolation functions for bending, and linear functions were used for axial and torsional deformations.

The "shuttle" is a steel plate of uniform thickness with a mass of 13.85 slugs. It is connected to the cable through a universal joint at point B. The $x_O y_O z_O$ frame is embedded in the shuttle with the origin at its center of mass as shown in Fig. 3. The center of mass is located 2.6708 ft from the rear of the shuttle in the x direction. Table 2 lists the values of the lumped masses attached to the plate and their respective locations. Table 3 identifies the location of the mast attachment to the shuttle as well as the universal joint location, both with respect to the $x_O y_O z_O$ frame. Note that the mast is attached below the rigid-body center of mass and the joint is located above the true center of mass. This joint location provides a horizontal static equilibrium orientation for the shuttle, which is the actual orientation for SCOLE. The total mass of the structure is 23.884 slugs, and the mass moment of inertia matrix about the universal joint is

$$I_B = \begin{bmatrix} 65.9409 & & \text{Symm} \\ -0.006082 & 89.0227 & \\ 7.4305 & 2.1118 & 87.5150 \end{bmatrix} (\text{slugs} \cdot \text{ft}^2)$$

B. Premaneuver Eigensolution

An eigensolution was obtained for the laboratory model of Fig. 3 with the structure in its static equilibrium state. The static deflection is plotted in Fig. 4. The natural frequencies are listed in the first column of Table 4, and several modes are

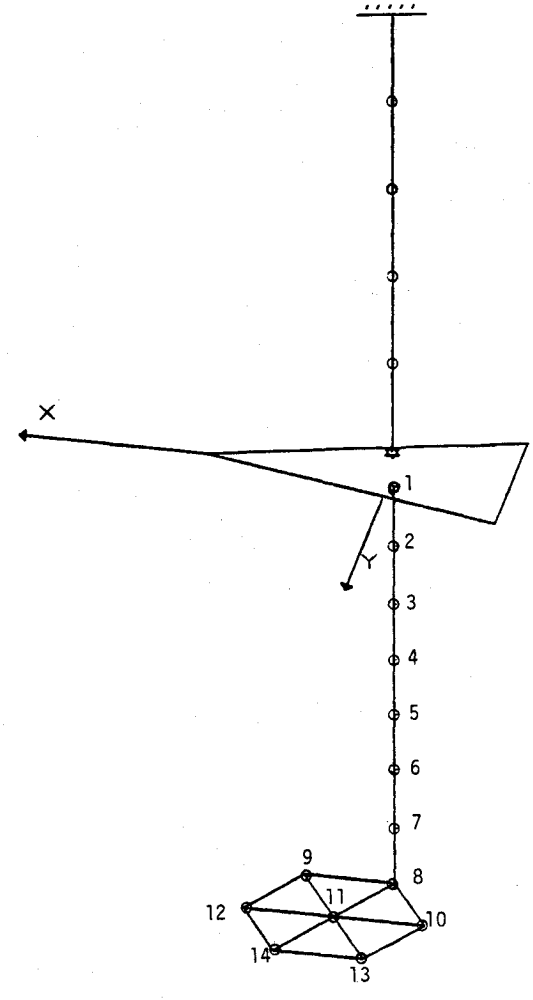

Fig. 3 SCOLE configuration showing nodal locations.

plotted in Figs. 5–8. The quantity FACT given in the plots is the scale factor used to amplify the deformations for plotting purposes. The static deflection is not included in the mode shapes. The universal joint is denoted by a star and the underformed structure by dashed lines. The view is from above and slightly behind the shuttle.

The appendage acts as if it were rigid in the first five modes. The first mode is a yaw rigid-body mode (rotation about the z_O axis). The second and third modes are combinations of pitch and roll, the former being mostly pitch (about the y_O axis). Modes 4 and 5 are pendulum modes consisting of rigid-body translations of the structure in the x_O and y_O directions. Modes 6 and 7 are the first bending modes of the appendage and exhibit deformations mainly in the $x_O z_O$ and $y_O z_O$ planes, respectively. Mode 8 is characterized by both bending and torsion of the mast. Modes 9 and 10 exhibit higher degrees of bending of the mast and perceptible deformations of the antenna, while mode 11 demonstrates an even more notable deformation of the antenna. Modes 12 and 13 are bending modes of the cable, with the structure appearing to be relatively unaffected. Modes 14 and 15 also exhibit notable deformations of the antenna. Mode 15 includes axial

Table 1 Element material properties

	Stiffness			Inertia	
	Bending	Torsion	Axial	Mass	Moment
	EI (lb · ft^2)	GJ (lb · ft^2)	EA (lb)	$\frac{m}{h}\left(\frac{\text{slugs}}{\text{ft}}\right)$	$\frac{I_{xx}}{m}$ (ft^2)
Cable	2.0	8.0	$3.3120(10^6)$	0.01160	$1.211(10^{-4})$
Mast	1,648	1,263	$3.9714(10^6)$	0.01391	$8.302(10^{-4})$
Antenna	557	411.65	$1.3397(10^6)$	0.00475	$8.327(10^{-4})$

Table 2 Lumped masses attached to the shuttle

	Mass (slugs)	Distance from point 0		
		x (ft)	y (ft)	z (ft)
Stack 1[a]	4.3478	−0.8177	−1.5312	1.4895
Stack 2[a]	4.3478	−0.8021	1.5625	1.4895
CMG	1.064	3.0938	−0.0625	0.6615

[a]Refer to masses added to adjust the position of the mass center.

Table 3 Mast and universal joint locations

	Distance from point 0		
	x (ft)	y (ft)	z (ft)
Rigid body mass center	−0.15385586	0.011609637	0.48217069
Mast attachment	−0.15385586	0.011609637	−0.375
True mass center	−0.15456184	0.010386841	0.48172838
Universal joint	−0.15456184	0.010386841	0.49366246

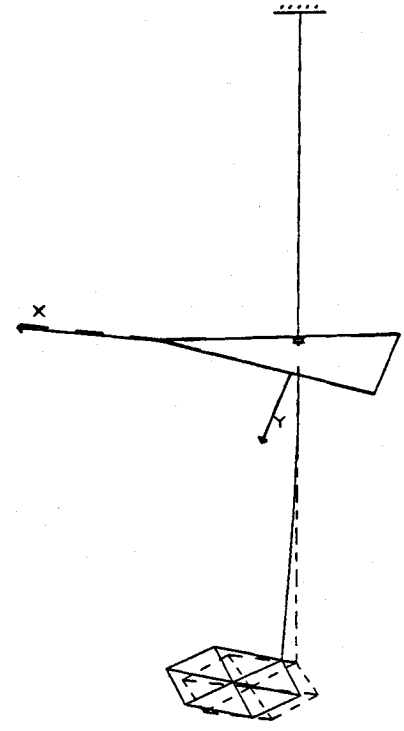

Fig. 5 Mode 6, FACT = 0.75, 1.021351 Hz.

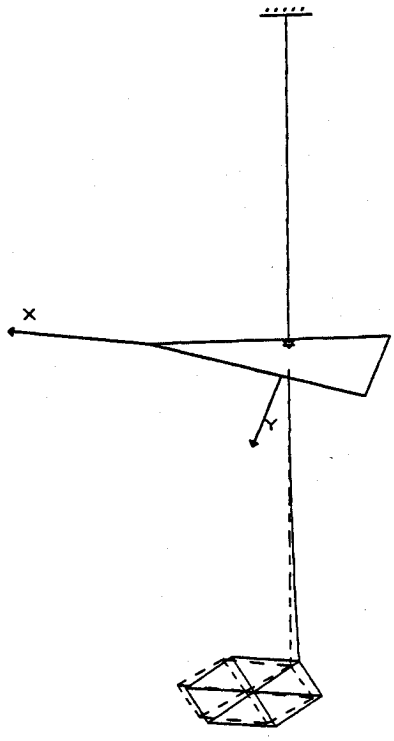

Fig. 4 Static deflection, FACT = 2.5.

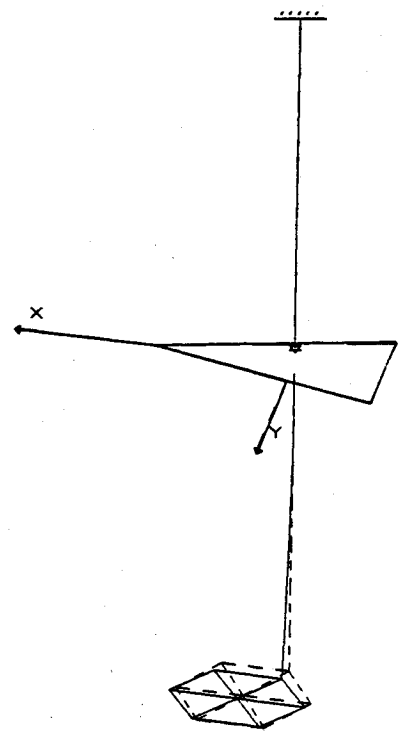

Fig. 6 Mode 7, FACT = 0.75, 1.092742 Hz.

motion of the cable, affecting the deflections of the mast and antenna.

Modes 16 and 17 are bending modes of the cable, like modes 12 and 13, with no perceptible effects on the structure. Hence, higher-order bending vibration of the cable has little effect on the spacecraft because the universal joint does not permit moment transmission from the cable to the spacecraft. As the mass of the cable approaches zero, the frequencies of the higher-order bending modes of the cable approach infinity. The second column of Table 4 contains the frequencies of the structure with the mass of the cable neglected. As expected, this approximation affects the remaining frequencies only slightly. The mass of the cable will be neglected in the sequel. Note that this approximation yields a time-invariant mass matrix as was assumed in Sec. VI.

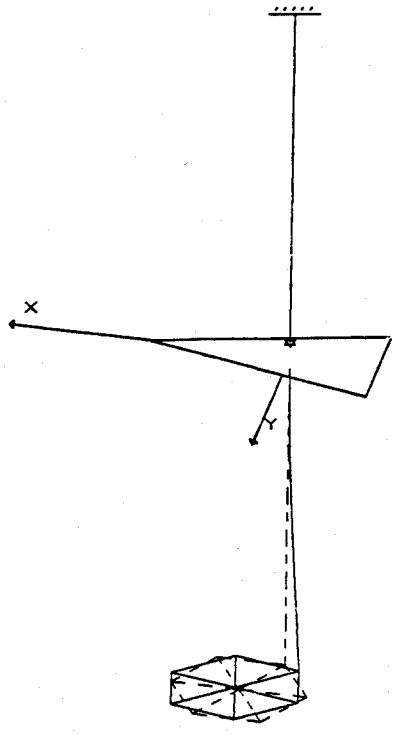

Fig. 7 Mode 8, FACT = 0.75, 2.869936 Hz.

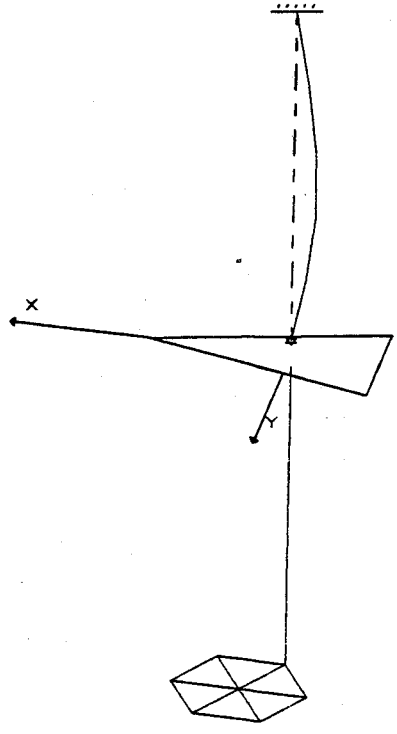

Fig. 8 Mode 12, FACT = 0.75, 11.997580 Hz.

Gravity has a great influence on the laboratory model. The natural frequencies of the spacecraft in a space environment, with no tether or gravitational effects, are listed in column three of Table 4. Note that there are now six zero frequencies corresponding to the rigid-body modes. All the frequencies are lower than the corresponding frequencies with gravity included because gravity has a stiffening effect. In fact, to further demonstrate the effect of gravity, the natural frequencies of the appendage cantilevered at the base are listed in Table 5. The first and second columns of Table 5 correspond to the cantilevered end of the mast lying above and below the mast, respectively. The direction of gravity with respect to the appendage has the greatest effect on the first two frequencies. The first two bending frequencies of the appendage are plotted vs the roll angle in Fig. 9 for the spacecraft in the laboratory. Zero degrees corresponds to the static equilibrium position of the structure. Hence, gravity strongly influences the stiffness of the appendage.

The last column of Table 4 demonstrates the error resulting from considering the antenna as rigid. Comparing this column with the column before last, we conclude that only the first two elastic modes of the appendage are relatively unaffected by this approximation.

C. Stability

For safety, a large degree of stability is important for the laboratory experiment. On the other hand, greater stability

Table 4 Natural frequencies (Hz)

	Equilibrium position		Zero gravity (space)	
Mode	Actual	Massless cable	Actual	Rigid Antenna
1	0.0	0.0	0.0	0.0
2	0.02661800	0.02661800	0.0	0.0
3	0.03335345	0.03335345	0.0	0.0
4	0.27527161	0.27550803	0.0	0.0
5	0.27528201	0.27551848	0.0	0.0
6	1.02135153	1.02136222	0.95626111	0.95781737
7	1.09274338	1.09275532	1.02205468	1.02304393
8	2.86993771	2.86993909	2.85798288	2.91078995
9	4.14099978	4.14100682	4.12238565	4.77249201
10	7.21202381	7.21203514	7.13573328	7.53400307
11	11.8888566	11.8892693	11.8067296	14.3285908
12	11.9975825	—	—	—
13	11.9979985	—	—	—
14	14.5271386	14.5271319	14.4703039	18.0655372
15	17.8807340	17.8965361	0.0	0.0
16	23.9951935	—	—	—
17	23.9951971	—	—	—
18	29.4618566	29.4618689	29.3765971	—
19	31.9790379	31.9790406	31.8650183	—
20	35.6083428	35.6083908	35.5681068	—

Table 5 Cantilever natural frequencies (Hz)

	Roll angle	
Mode	0 deg	180 deg
1	0.90329379	0.74059481
2	0.92231250	0.74130235
3	2.85838001	2.84157907
4	4.11631152	4.06401370
5	7.18829155	7.03295932
6	11.8569533	11.6900310
7	14.5078152	14.3982264
8	29.4282394	29.2763643
9	31.9410827	31.7363829

results in increased control effort to combat gravity during a maneuver. Hence, a stability analysis is essential.

The stable region during a roll maneuver is defined as the range of the roll angle while the static stiffness matrix remains positive semidefinite. A positive semidefinite stiffness matrix implies nonnegative eigenvalues, because the mass matrix is positive definite. The location of the universal joint with respect to the center of mass is the critical parameter for stability. Of course, as the structure changes position with respect to the direction of gravity, the spacecraft deforms and the center of mass moves.

Let z_B denote the distance in the z_O direction from the shuttle's center of mass O to the universal joint B. Note that the rigid-body center of mass is listed in Table 3. The first three eigenvalues are plotted vs the roll angle in Figs. 10a–10c, each figure corresponding to a different value of z_B. Note that in all three cases, one and only one mode is always marginally stable. The first two modes are unstable at 0 deg for z_{B1}, as evidenced by Fig. 10a. A slight increase in z_B from z_{B1} to z_{B2} yields stability in the region -35 deg $< \theta <$ 20 deg. A further increase in z_B to z_{B3} yields an even wider stability range. Note that the plots are not symmetric because the flexible appendage is not symmetric. Physically, when the first mode becomes unstable, the structure begins to slew about the z_O axis if no control force is applied. When the next mode becomes unstable, the structure continues to roll with no external force application, so that it will begin to turn upside down.

Considering the plot for $z_B = z_{B1}$, if stabilizing control is applied, the structure can be rotated from $\theta = -40$ to $\theta = 30$ deg with little effort to combat gravity. In fact, three-dimensional stability curves, considering both pitch and roll, can be useful in determining an even more advantageous maneuver trajectory. The laboratory model used corresponds to $z_B = z_{B2}$.

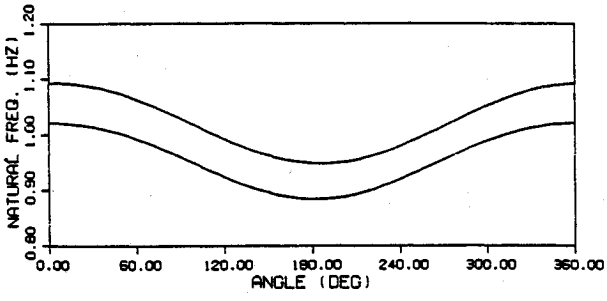

Fig. 9 First two bending frequencies vs roll angle.

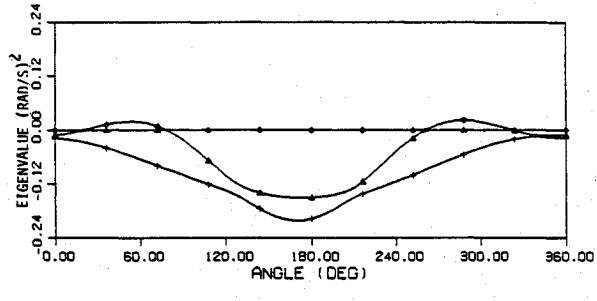

a) $Z_{B1} = 0.490662$ ft

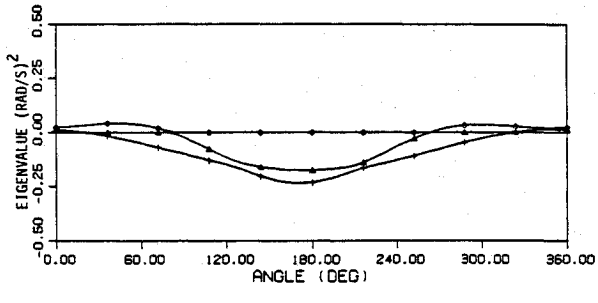

b) $Z_{B2} = 0.493662$ ft

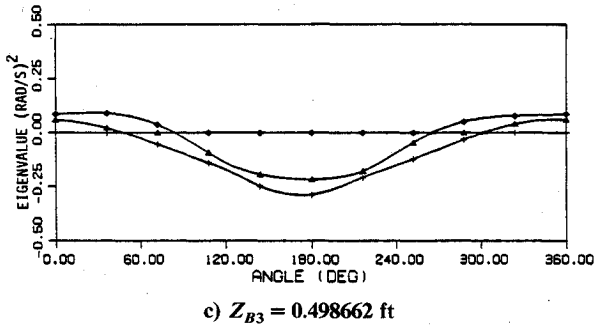

c) $Z_{B3} = 0.498662$ ft

Fig. 10 First three eigenvalues vs roll angle.

D. Rotational Maneuvers

The maneuver strategy of Ref. 2 was applied to the rigid-body model of the spacecraft. The actuator response was assumed to be of first-order as in Eq. (19), with $a = -10$ and $b = 1$.

Figures 11a–11c show the history of a minimum-time roll maneuver from 0–20 deg with $M_{\max} = 5$ ft·lb. Both continu-

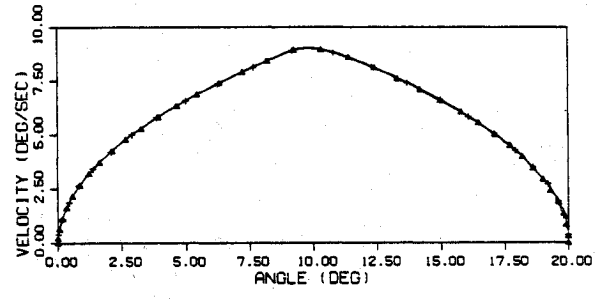

a) Angular velocity vs angle

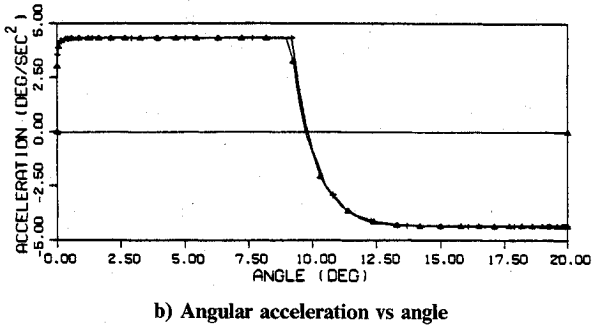

b) Angular acceleration vs angle

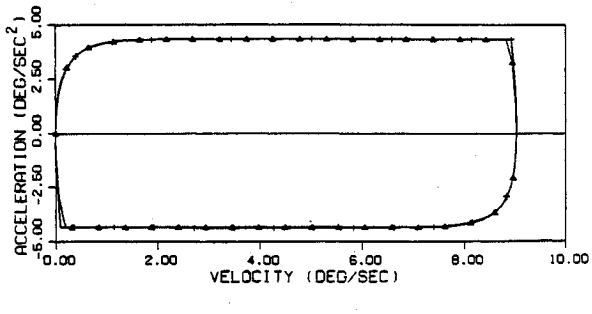

c) Angular acceleration vs velocity

Fig. 11 Maneuver strategy for 20-deg roll with $M_{\max} = 5$ ft·lb.

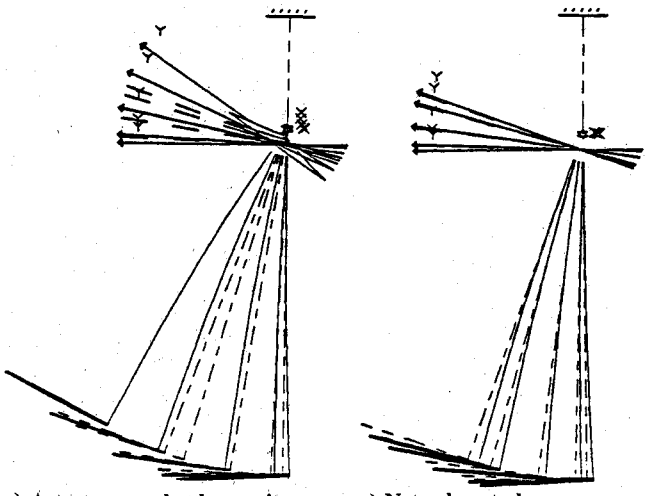

a) Actuators on shuttle, gravity included in maneuver policy

c) Natural control

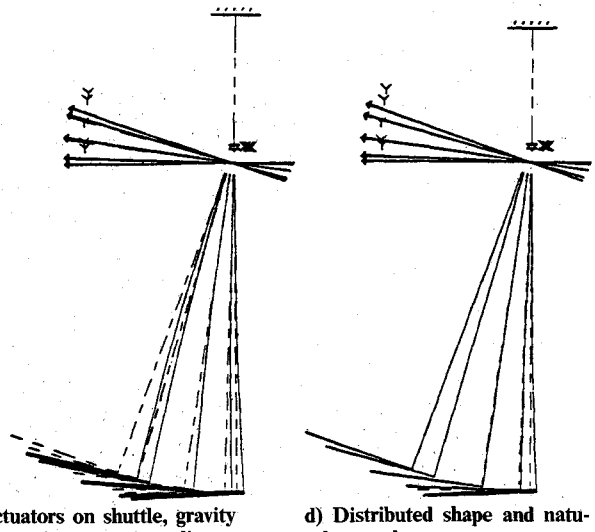

b) Actuators on shuttle, gravity neglected in maneuver policy

d) Distributed shape and natural controls

Fig. 12 Time-lapse plots of 20-deg maneuver in laboratory, FACT = 1.0.

ous- and discrete-time switching histories are plotted in these figures, with the + symbol denoting discrete switching and the Δ symbol denoting continuous switching time histories. There is a perceptible difference only at the switching states. The effect of the actuator response is to smooth the curves at the switching states. If the actuator response is instantaneous, the acceleration is discontinuous.

With the present configuration of the SCOLE model, the only equilibrium position is the 0-deg position, so that a departure from this angle requires moments to counteract gravity, even when the structure is at rest. First, the laboratory model is rotated through the 20-deg roll maneuver as if it were rigid, with the maneuver strategy accounting for the effects of gravity. Next, the gravitational correction is removed from the maneuver moments and forces and the rotation is repeated. Vibration control is then added to the control strategy, and the need for shape control is demonstrated. Finally, the structure is maneuvered using both vibration and shape control, which together produce the desired performance. The first 12 modes are simulated, and the initial state is the static equilibrium configuration.

Figure 12a is a time-lapse plot of the laboratory model during the maneuver in which the body is assumed to be rigid. The maneuver strategy was modified to include moments to offset the gravitational torques. No vibrational controls were used, and the maneuver was performed with actuators located at the shuttle. Because the appendage deforms during the

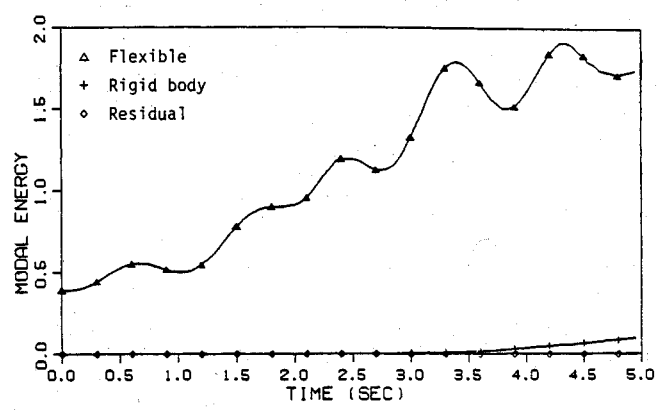

a) Maneuver control policy

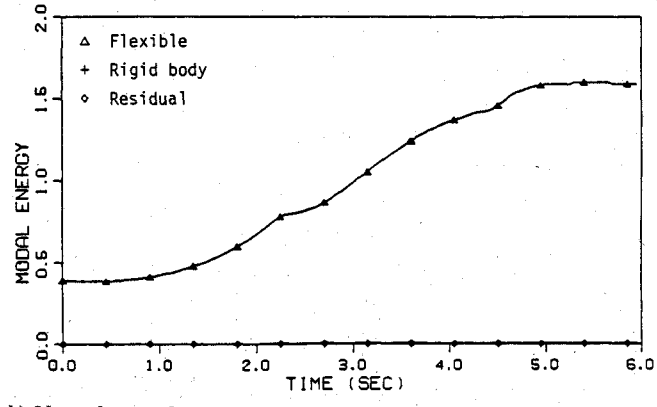

b) Natural control

Fig. 13 Energy during 20-deg roll maneuver.

maneuver, the rigid assumption for moment calculations results in an overcompensation for the gravity torques and errors on the order of the maneuver angle itself. Hence, the deformation of the appendage affects the moments necessary to counterbalance the gravitational torques strongly.

Figure 12b is a time-lapse plot of the laboratory model during the same rotation in which the maneuver strategy was followed with no correction for gravity. Again, no vibration control was used, and the moments were produced with actuators located on the shuttle. Little rigid-body error has resulted, but the deformation of the appendage due to gravity is large. Figure 13a illustrates the energy in the system vs time. The mode mainly excited is the second flexible mode, mode 7.

Next, natural control implemented with distributed actuators and sensors was applied to the spacecraft along with the 20-deg maneuver strategy. The constants in the performance functional were chosen as $R = 0.01$ and $q = 1.0$ for all nine controlled modes. Figure 12c is the corresponding time-lapse plot. The appendage still lags its desired position for this case, though the error has been reduced. A comparison of Figs. 13a and 13b shows that both the energy fluctuations during the maneuver and the steady-state energy level have been reduced with the addition of natural control. The steady-state error is caused by the gravitational force.

Natural control is chiefly a vibration suppressor, not a shape controller. A decrease in the weight R increases all the gains, not just the displacement control gain, which would be the case in shape control. Hence, the addition of shape control is necessary to counterbalance the gravitational force without affecting the desired active damping. The distribution of the gravitational force depends on the mass distribution of the structure, which is known reasonably well. Thus, the shape control force can be open-loop. Note that, as demonstrated, natural control does provide a small amount of shape control by virtue of displacement control. Hence, it can partially offset small steady-state errors.

The torques required to counteract gravity in the case in which the structure is regarded as rigid is also included in the shape control force. The gravitational force is distributed over the entire structure. Hence, if precise shape control is desired, the control force must also be distributed, or at least it must be produced by a large number of discrete actuators dispersed throughout the structure.

A distributed shape control force was applied along with the maneuver controls but with no vibration control. Figure 14a is the corresponding plot of energy vs time. The energy fluctuates but the mean energy level rises only slightly with time. Without vibration control, the system is actually unstable, which explains the rising mean energy level. Hence, vibration control is needed to stabilize the system as well as to suppress the vibration. The command moments at the universal joint are plotted in Fig. 14b. Note that the magnitude of the shape control moment dwarfs the maneuver moment. A steady-state moment of about -26 ft · lb at the shuttle is required to maintain the steady-state configuration.

Next, natural control implemented with distributed actuators and sensors was applied to the structure along with the shape and maneuver controls. The corresponding time-lapse plot is shown in Fig. 12d. The performance is excellent, as can be seen from the plot of the system energy vs time of Fig. 15a. The antenna rotations are virtually nullified soon after the end of the maneuver. The most active of the antenna vibrational rotations is that about the x_O axis, which is shown in Fig. 15b.

As demonstrated in Ref. 3, distributed control approximated by means of a relatively few actuators produces excellent vibration control. However, applying open-loop shape control with this technique and a finite number of actuators results in a steady-state error. Increasing the gains can reduce this error but results in some undesirable deformation. An alternative is to use natural control to help reduce the steady-state error with the shape control supporting most of the steady-state load. Note that when the vibration of the structure has subsided, the only feedback force for natural control

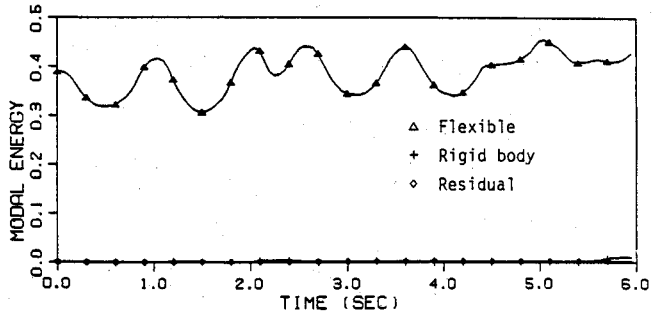

a) Energy

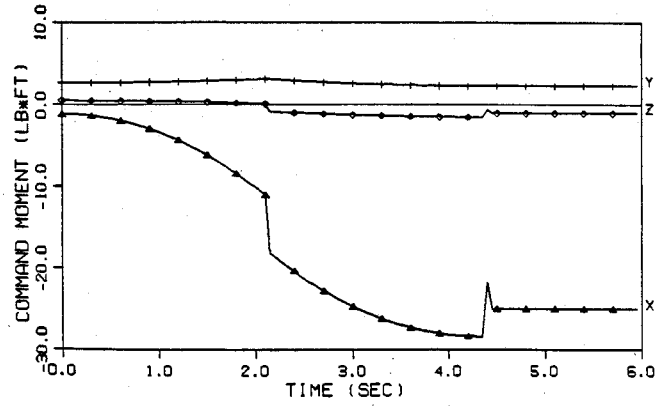

b) Command moments on shuttle

Fig. 14 Distributed shape control opposing gravity during 20-deg maneuver.

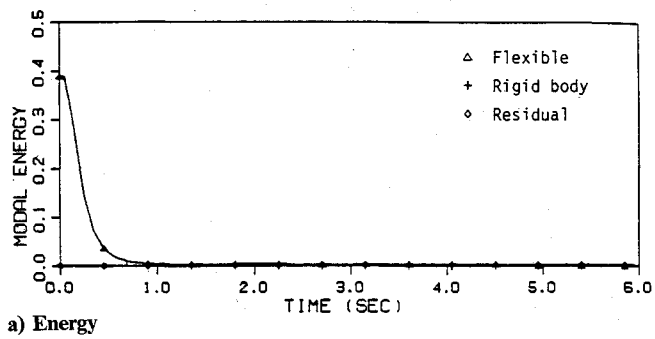

a) Energy

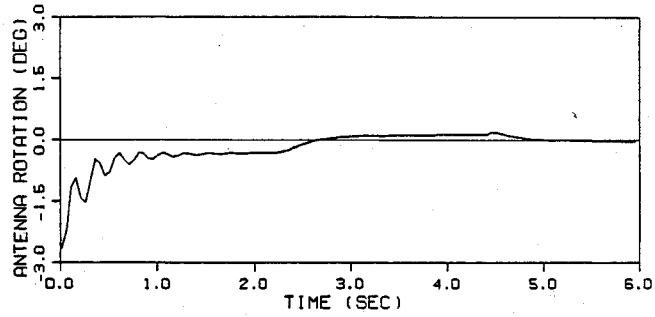

b) Rotation of antenna hub in x_O direction

Fig. 15 Distributed shape and natural control applied during 20-deg maneuver.

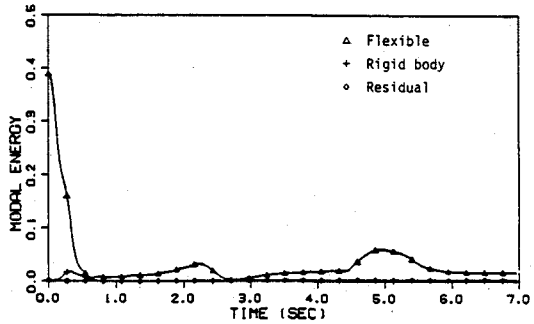

a) Energy

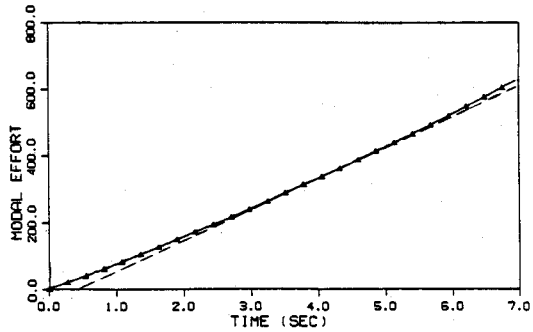

b) Effort

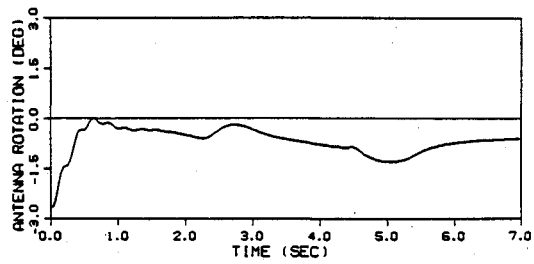

c) Antenna hub rotation in x_O direction

Fig. 16 Projected control of 20-deg roll with R beginning to decrease at $t = 5.0$ s.

is due to the displacement control, so that the process reduces to shape control. Hence, when precise aiming of the antenna is required, R can be decreased, so that the displacement gain (along with the other gains) is increased. In this manner, the steady-state error can be reduced to within the desired tolerance and the antenna locked on target.

Natural control, shape control, and maneuver control were all implemented with 23 actuators approximating distributed control. A scheme involving discrete sensors approximating distributed sensors for modal estimation was also used, where the sensors were collocated with the actuators. Referring to Fig. 3, the actuator and sensor locations were as follows: thrusters and torquers in the x_O, y_O, and z_O directions at the universal joint, torquers in the x_O direction at node 4 and the y_O direction at node 6, thrusters in the x_O, y_O, and z_O directions at nodes 8, 11, and 14, and thrusters in the x_O direction at node 12 and the y_O direction at node 13.

The maneuver strategy ends at $t = 4.77$ s. Starting at $t = 5.00$ s, R was incrementally decreased by 10% at each sampling time from $R = 0.01$ to $R = 0.0005$. The corresponding plots of the system energy vs time are shown in Fig. 16a, and the corresponding plot of the antenna vibrational rotation in the x_O direction is shown in Fig. 16c. By increasing the gains at $t = 5.00$ s, the steady-state error is reduced by more than one-half within 2 s. A considerable amount of effort is required to provide shape control, as illustrated by Fig. 16b, which is a plot of the modal effort vs time. A dashed straight line has been added to the plot to accentuate the increase in slope at $t = 5.00$ s corresponding to the increase in control gains.

X. Conclusions

The perturbation method permits the design of a maneuver strategy independently of the vibration problem, thus rendering the task of maneuvering vibration control considerably easier. The mass matrix is time-invariant for the laboratory model (as it is for the structure in space) if the mass of the tether is neglected. This is equivalent to neglecting the tether higher bending modes, which is reasonable, because the higher bending modes of the cable involve little "spacecraft" participation. Balancing gravity during a maneuver presents difficulties unique to the laboratory, because the cable provides support concentrated at a point. Stability of the structure during the maneuver is a prime factor due to considerations of safety and minimization of maneuver effort. Note that a maneuver about the axis of the cable obviates the problem of combating the effects of gravity. Any axis of the spacecraft can be made to correspond to the cable axis by adjusting the universal joint location relative to the center of mass. The maneuver and vibration control techniques of Refs. 2 and 3 perform well for the laboratory experiment, but an additional shape control may be needed. Shape control can require much more effort than mere vibration control, and precise shape control may not be feasible for the laboratory experiment. An alternative is to permit the appendage to deform under gravity during the maneuver, retaining mere vibration control. A strategy providing control of the orientation and shape of the antenna only may result in a reduction of shape control effort.

Acknowledgments

Supported by the NASA Research Grant NAG-1-225 sponsored by the Spacecraft Control Branch, Langley Research Center, and monitored by Jeffrey P. Williams.

References

[1]Meirovitch, L. and Quinn, R.D., "Equations of Motion for Maneuvering Flexible Spacecraft," *Journal of Guidance, Control, and Dynamics,* Vol. 10, Sept.-Oct. 1987, pp. 453-465.

[2]Quinn, R.D. and Meirovitch, L. "Equations for the Vibration of Slewing Flexible Spacecraft," AIAA Paper 86-0906, May 1986.

[3]Meirovitch, L. and Quinn, R.D., "Maneuvering and Vibration Control of Flexible Spacecraft," *Journal of the Astronautical Sciences*, Vol. 35, 1987, pp. 301-328.

[4]Turner, J.D. and Junkins, J.L., "Optimal Large-Angle Single-Axis Rotational Maneuvers of Flexible Spacecraft," *Journal of Guidance and Control,* Vol. 3, Nov.-Dec. 1980, pp. 578-585.

[5]Breakwell, J.A., "Optimal Feedback Slewing of Flexible Spacecraft," *Journal of Guidance and Control,* Vol. 4, Sept.-Oct. 1981, pp. 472-479.

[6]Turner, J.D. and Chun, H.M., "Optimal Distributed Control of a Flexible Spacecraft During a Large-Angle Maneuver," *Journal of Guidance, Control, and Dynamics,* Vol. 7, May-June 1984, pp. 257-264.

[7]Baruh H. and Silverberg, L., "Maneuver of Distributed Spacecraft," AIAA Paper 84-1952, Aug. 1984.

[8]Meirovitch, L., Baruh, H., Mongomery, R.C., and Williams, J.P., "Nonlinear Natural Control of an Experimental Beam," *Journal of Guidance, Control, and Dynamics,* Vol. 7, July-Aug. 1984, pp. 437-442.

[9]Meirovitch, L. and Shenhar, J., "Control of Large Flexible Spacecraft by the Independent Modal-Space Control Method," NASA CR-3760, Jan. 1984.

[10]Meirovitch, L., *Computational Methods in Structural Dynamics*, Sijthoff & Noordhoff, The Netherlands, 1980.

[11]Meirovitch, L. and Baruh, H., "Control of Self-Adjoint Distributed-Parameter Systems," *Journal of Guidance, Control, and Dynamics*, Vol. 5, Jan.-Feb. 1982, pp. 60-66.

[12]Meirovitch, L. and Silverberg, L.M., "Globally Optimal Control of Self-Adjoint Distributed Systems," *Optimal Control Applications and Methods*, Vol. 4, 1983, pp. 365-386.

[13]Silverberg, L., "Uniform Damping Control of Spacecraft," *Proceedings of the Fifth VPI&SU/AIAA Symposium on Dynamics and Control of Large Structures,* AIAA, New York, June 1985; also *Journal of Guidance, Control, and Dynamics,* Vol. 9, 1986, pp. 221-227.